Article:

Chapman, T, Clarke, GL, Piazolo, S orcid.org/0000-0001-7723-8170 et al. (1 more author) (2019) Inefficient high-temperature metamorphism in orthogneiss. American Mineralogist, 104 (1). pp. 17-30. ISSN 0003-004X

https://doi.org/10.2138/am-2019-6503

DOI: https://doi.org/10.2138/am-2018-6503

Revision 1

Quantifying the proportions of relict igneous and metamorphic minerals in orthogneiss: linking metamorphic efficiency to deformation

Timothy Chapman[1]*, Geoffrey L. Clarke[1], Sandra Piazolo[2+] and Nathan R. Daczko[2].

[1]School of Geosciences, The University of Sydney, NSW, 2006, Australia

[2]ARC Centre of Excellence for Core to Crust Fluid Systems and GEMOC, Department of Earth and Planetary Sciences, Macquarie University, NSW, 2109, Australia

[+] Current address: School of Earth and Environment, University of Leeds, United Kingdom

*Corresponding author: t.chapman@sydney.edu.au

ABSTRACT

A novel method utilising crystallographic orientation and mineral chemistry data, based on large-scale electron back-scatter diffraction (EBSD) and microbeam analysis, quantifies the proportion of relict igneous and neoblastic minerals forming variably deformed high-grade orthogneiss. The Cretaceous orthogneiss from Fiordland, New Zealand, comprises intermediate omphacite granulite interlayered with basic eclogite, which were metamorphosed and deformed at $T \approx 850°C$ and $P \approx 1.8$ GPa after protolith cooling. Detailed mapping of microstructural and physiochemical relations in two strain profiles through subtly distinct intermediate protoliths indicates that up to 32% of the orthogneiss mineralogy is igneous, with the remainder being metamorphic. Domains dominated by igneous minerals occur preferentially in strain shadows to eclogite pods. Distinct metamorphic stages can be identified by texture and chemistry, and were at least partially controlled by strain magnitude. At the grain-scale, the coupling of metamorphism and crystal plastic deformation appears to have permitted efficient transformation of an originally igneous assemblage. The effective distinction between igneous *and* metamorphic paragenesis and their links to deformation

history enables greater clarity in interpretations of the make-up of the crust and their causal influence on lithospheric scale processes.

Keywords: neoblasts, EBSD, recrystallization, strain, tectonometamorphism, microstructure

INTRODUCTION

It is generally considered that elevated temperature conditions in Earth's crust (e.g. >750°C) are accompanied by widespread metamorphic equilibration, on account of elemental diffusion distances being comparable to, or larger than the grain-scale (Powell et al., 2005). Typically, metamorphic transformation is aided by pervasive deformation and the abundance of fluid (H_2O or melt: Štipská & Powell, 2005; Powell et al., 2005). However, the persistence of high proportions of metastable minerals in orthogneiss exhumed from the lower crust is common (e.g. Austrheim et al., 1997, Štipská & Powell, 2005; Racek et al., 2008). In circumstances involving inhibited metamorphism, parts of a given rock can be incompletely equilibrated (Vernon et al., 2008, 2012). The efficiency and scale of metamorphic equilibration must be queried in the context of results from analogue experiments and mineral equilibria modelling to provide a robust understanding of the inferred petrogenesis (Powell et al., 2005; Štípská & Powell, 2005). In turn, mineral chemistry and texture can be used to recover dynamic changes in extrinsic conditions that can be extrapolated to make geodynamic inferences (Marmo et al., 2002; Chapman et al., 2017).

In circumstances of inefficient metamorphism, sites of mineral reaction can be highly localised (e.g. Austrheim et al., 1997; Jamtveit et al., 2000) and can contribute to the partitioning of strain during deformation (Williams et al., 2014). A dynamic feedback between reaction kinetics and recrystallization mechanisms can accentuate reaction localisation and mechanical differentiation (Yund & Tullis, 1991; Stünitz, 1998; Piazolo et al., 2016). Most studies of inhibited metamorphism focus on linking mineralogical change to brittle failure and/or fluid ingress (e.g. Jamtveit et al., 2000); there are few studies that assess the role of dynamic recrystallization during ductile deformation (e.g. Svahnberg & Piazolo, 2010; Satsukawa et al., 2015). Changes in mineralogy have a direct bearing on the rheology and density of the lithosphere (Jackson et al., 2004; Bürgmann & Dresen, 2008; Chapman et al., 2017). It is commonly assumed in the application of geodynamic models that metamorphism in the lower crust is highly efficient, yet this is an over simplification. Inefficient metamorphism is commonly associated with low heat- and/or fluid-flux environments, as occurs in cratons, but can also occur in orogenic settings due to changes in key extrinsic variables (Štípská & Powell, 2005; Racek et al., 2008; Daczko et al., 2009). There is a need to establish a method to calculate the proportions of igneous material in partially metamorphosed and deformed granitoids from such settings.

In this paper, we quantify the proportions of igneous and metamorphic minerals in a case study of rocks that show partial to complete metamorphic transformation at high-T and high-P conditions ($T \approx 850$°C and $P \approx 1.8$ GPa). We use unique exposures of rocks exhumed from lower crustal conditions in Fiordland, New Zealand, that preserve composite layered plutons, patchily deformed and transformed to granulite and eclogite (De Paoli et al., 2009, 2012). Metamorphism and deformation occurred immediately after, and plausibly concurrently with, the high-pressure emplacement of the plutons, but was spatially restricted. This example conflicts with most of the generalisations of lower crust behaviour through: (1) preserving igneous minerals and textures that metastably persisted at high-T conditions; largely because of (2) strain localization. A method to quantify the proportions of igneous relicts and the degree of metamorphic growth is established using mineral structural timing relationships, quantitative crystallographic orientation analysis coupled with mineral chemistry. Mineralogy outlined by the technique includes: (1) phenocrystal relicts, that have distinctive orientation and highly distributed lattice strain; (2) neoblastic grains associated with deformation structures that can be distinguished from igneous reactants by chemistry,

This is a preprint, the final version is subject to change, of the American Mineralogist (MSA)
Cite as Authors (Year) Title. American Mineralogist, in press.
DOI: https://doi.org/10.2138/am-2018-6503

crystallographic orientation characteristics and grain size; and (3) partially modified igneous grains, that underwent chemical change in localised (micron to mm-scale) regions associated with deformation structure. The primary focus of this study is to distinguish neoblasts from igneous (protolith) material. It is shown that, despite *PT* conditions considered amenable to metamorphic conversion and crystal plastic deformation, metamorphic transformation and neocrystallization was inhibited in up to 32% of the rock volume.

THE BREAKSEA ORTHOGNEISS

The Fiordland region on the South Island of New Zealand preserves a disrupted section of the Late Cretaceous palaeo-Pacific Gondwanan margin. Mafic to intermediate rocks of the Western Fiordland Orthogneiss (WFO) are parts of a larger Cretaceous arc batholith (*c*. 125–111 Ma: Bradshaw, 1989; Allibone et al., 2009; Milan et al., 2016, 2017). The Breaksea Orthogneiss is the highest-pressure unit in the WFO (Fig. 1a), preserving omphacite granulite and eclogite ($T \approx 850°C$ and $P \approx 1.8$ GPa: De Paoli et al., 2009). It is composite, being formed mostly of monzodioritic to monzogabbroic omphacite granulite (*c*. 60–65%), cognate monzodioritic omphacite–orthopyroxene granulite (*c*. 5–10%), and cumulate basite (now eclogite; *c*. 25%), clinopyroxenite and garnetite (*c*. 5%) (De Paoli et al., 2009; Clarke et al., 2013; Chapman et al., 2015).

This layered protolith is inferred to have been emplaced at high-*P* conditions (1.8–2.0 GPa) between *c*. 124 and 115 Ma (Milan et al., 2016; Stowell et al., 2017). It was incompletely metamorphosed and deformed (D_1) during cooling, initially at the emplacement depth (Table 1: Chapman et al., 2017). The presence of mutually cross-cutting igneous veins and S_1 folia are consistent with the D_1 event having occurred late in the protolith crystallization. The S_1 foliation commonly includes steep S-L fabrics that transpose planar igneous layering (Chapman et al., 2017) and is deformed into metre to km-scale concentric domes (Betka & Klepeis, 2013). Post-S_1 decompression to lower grade conditions ($P \approx 1.0$–

1.4 GPa and $T \approx$ 650–750°C) is recorded by diopside and albite symplectite that pseudomorph S_1 omphacite (De Paoli et al., 2009) and corresponds to a period of extensional dome formation (Klepeis et al., 2016; Chapman et al., 2017). Localized D_2 amphibolite facies shear zones cut igneous layering and S_1 folia, and are thought to have formed during orogenic collapse possibly coupled with root foundering (Fig. 1a; Klepeis et al., 2007; Chapman et al., 2017).

The spectrum of whole-rock compositions in the main rock types of the Breaksea Orthogneiss define linear first-order trends in Harker plots from peridotgabbro to monzodiorite (De Paoli et al., 2009, 2012). These compositional variations are mostly attributed to cumulate processes and magma redox conditions that preceded high-grade deformation (Clarke et al., 2013; Chapman et al., 2015; Cyprych et al., 2017). Interlayered near-monomineralic garnetite and clinopyroxenite retain delicate cumulate microstructure and unique crystallographic fabrics (Fig. S1: Clarke et al., 2013; Cyprych et al., 2017). Igneous clinopyroxene and garnet are well preserved in these ultra-basic cumulate layers; they have rare earth element (REE) chemistry that overlap with that of clinopyroxene and garnet in basic and intermediate protoliths (Clarke et al., 2013). A commonality in mineral REE chemistry coupled with the preservation of igneous microstructure supports the interpretation of the basic and ultrabasic components being cumulates of basic to intermediate magmatism (Fig. S1: Clarke et al., 2013).

Mineral chemical relationships identified in ultrabasic components of the Breaksea Orthogneiss can be partially extended into its felsic components. However, metamorphism was more pervasive in felsic portions of the orthogneiss, presumably because of rheological distinctions (Chapman et al., 2015; Miranda & Klepeis, 2016). Igneous and metamorphic (neoblastic) garnet can be distinguished by the following textural and chemical features (after Clarke et al., 2013). Large igneous garnet and omphacite occur as euhedral grains in cm-scale

This is a preprint, the final version is subject to change, of the American Mineralogist (MSA)
Cite as Authors (Year) Title. American Mineralogist, in press.
DOI: https://doi.org/10.2138/am-2018-6503

clusters, with garnet heavy-REE-enriched patterns overlapping with those of igneous garnet in eclogite and garnetite. Garnet phenocrysts also have rutile exsolution and lack positive Eu anomalies, consistent with their growth from a high-*T* liquid (>1000°C: Chapman et al., 2017) and inconsistent with peritectic growth from prograde incongruent partial melting (Clarke et al., 2013). Idioblastic metamorphic garnet is commonly symplectic with quartz, forms coronae to omphacite and plagioclase, is heavy-REE depleted and has a positive Eu anomaly. Other rock-forming minerals have relationships that are ambiguous, but are likely to have involved a combination of igneous and metamorphic histories dependent on strain intensity. Foliated assemblages of omphacite, garnet, plagioclase, kyanite and rutile are consistent with metamorphism at conditions of the omphacite granulite sub-facies (De Paoli et al., 2012; Clarke et al., 2013). Other portions of the felsic rocks, typically in low-strain domains, have igneous grain shapes with compositions that are consistent with a parental magma crystallising Ca–Na clinopyroxene with or without garnet or orthopyroxene (Chapman et al., 2015). The extent of neocrystallization in the felsic lower crustal rocks is the focus of this study.

Field Relationships

The primary igneous fabric at Breaksea Tops involves both gradational and sharp contacts between distinct layers in the intermediate rocks and the decimetre-scale cumulate pods, that are defined by variations in the proportions of garnet, clinopyroxene, orthopyroxene and plagioclase. The layering is locally transposed into a moderately dipping (>65°), north-west-striking gneissic foliation (S_1) with an associated L_1 mineral stretching lineation plunging towards the southeast (Fig. 1a). The gneissic fabric is defined by elongate and aligned cm-scale garnet–pyroxene grain clusters in intermediate gneiss ("mafic clusters"). Deformation of S_1 folia into concentric domes is not observed at the Breaksea Tops and appear to be spatially related to the extensional D_2 Resolution Island Shear Zone (RISZ) in Breaksea

Sound (Fig. 1a: Betka & Klepeis, 2013; Klepeis et al., 2016). At Breaksea Tops, S_1 folia are deflected around competent basite pods, with the intensity of the lineation increasing away from the pods (Fig. 1b). Decimetre- to decametre-scale low-strain domains commonly occur in strain shadows of the basic components (Fig. 1b), where igneous layering that lacks a penetrative mineral lineation is cut by S_1.

Fifteen orientated samples were collected from the layered parts of the monzogabbroic to monzodioritic gneiss from a ridge transect at the Breaksea Tops (Fig. 1a). The sample suite includes a transition from rocks with shallowly-dipping igneous layering, to those with well-developed moderately-dipping S_1–L_1 fabrics (Fig. 2a). The distinction of magmatic and tectonic fabrics, and in particular the aspect ratio of minerals defining L_1, was used to assess strain (Fig. 2b; Flinn, 1965). Modal layering resulted in the preservation of two strain series across subtly distinct protoliths: (1) a monzogabbro that records low to intermediate strain; and (2) a monzodiorite that records intermediate to high strain. Detailed mapping of the samples was used to determine the area percentage of each protolith and strain type across the Breaksea Top transect (Fig. 2b). Approximately 27% of the outcrop involved monzogabbroic gneiss that records largely low strain magnitude. It transitions into intermediate L_1–S_1 fabrics in ~ 40% of the outcrop area. High-strain monzodioritic gneiss, marked by linear (L_1>S_1) fabrics and coronitic garnet development, covers ~ 20% of the outcrop area. Protoliths to these zones are preserved as intermediate strain layers in only 13% of the outcrop. A series of four samples were selected for detailed petrographic and microstructural investigation (Fig. 2a).

METHODS

Optical petrographic and microstructural observations were coupled with focused (areas of *c.* 2 x 2 mm) and large-scale (areas of 1 x 1.5 cm) quantitative crystallographic orientation mapping using the electron back-scatter diffraction (EBSD) technique (Prior et al. 1999).

Mineral chemical analysis was undertaken on the same samples and within the region of EBSD mapping. All thin sections were prepared perpendicular to the foliation (XY plane) and parallel to the lineation (Z direction). Aspect ratios (*AR* = long/short axes) of mafic grain clusters on planes parallel to the lineation (XZ plane) were used to quantify strain intensity together with $D = \sqrt{[\ln(X/Y)^2 + \ln(Y/Z)^2]}$ (Fig. 2b) following Flinn (1965).

Quantitative crystallographic orientation analysis

Electron back-scatter diffraction (EBSD) investigation was performed using a Zeiss EVO Ma 15 scanning electron microscope (SEM) housed at Macquarie Geoanalytical at Macquarie University, Sydney. Additional data was also collected on a Zeiss Ultra Plus SEM at the Australian Centre for Microscopy and Microanalysis (ACMM) at the University of Sydney. Etched polished thick sections (*c*. 100 μm) were analysed at an accelerating voltage of 20–30 kV, with a beam current of 8 nA and a working distance of ~9–14 mm. Electron backscatter diffraction patterns were automatically acquired and indexed using Oxford Instruments AzTEC software (https://www.oxford-instruments.com/). The EBSD patterns were collected in regular grids where the sampling step size varied from 2 to 8 μm for detailed microstructural areas and 15 to 18 μm for whole thin-section mapping. For each data point the crystallographic orientation of the mineral was determined based on Kikuchi diffraction patterns (Prior et al., 1999). Post-processing was undertaken in the Channel 5 TANGO software (Oxford Instruments) following procedures described by Prior et al. (2002) and Piazolo et al. (2006). The post-processing methods are designed to remove false data (misidentified during scanning) and to enhance data continuity over the microstructures in relation to the overall scan index rate. Modal abundances were determined using volume calculations on thin-section scale EBSD maps in Channel 5 (Table 2). The calculations were compared to mineral equilibria modelling results of Chapman et al. (2017) to assess the potential extent of equilibration.

In the following analysis, grains are defined as areas enclosed by boundaries of greater than 10° of misorientation, referring to the distortion of the crystalline lattice; boundaries with misorientations less than 10° but greater than 2° are referred to as low-angle boundaries. If the low-angle boundaries have crystallographic rotational characteristics and lattice distortions consistent with recovery they are defined as subgrain boundaries (sgb). Grain internal strain was estimated following Piazolo et al. (2006), where a grain with an average internal misorientation of <1° is denoted as substructure-free.

We utilize the strength of the crystallographic preferred orientation (CPO) as an additional measure of strain intensity. This has been evaluated by calculating the texture index (*J*: after Bunge, 1982) in the MTEX software package (Mainprice et al. 2011) for omphacite and plagioclase. The texture index has a value of one for a random distribution and an infinite value for a single crystal (Bunge, 1982).

Mineral chemistry

Mineral chemical data for the studied samples and specific microstructures presented here (Table 3) complements detail mineral chemical relationships already published on the Breaksea Orthogneiss (De Paoli et al., 2009; Clarke et al., 2013; Chapman et al., 2015). The major element content of the rock-forming minerals was determined using the same polished thin/thick sections as those for EBSD and a CAMEBAX SX100 electron microprobe (EMP) housed at Macquarie Geoanalytical. Operating conditions for the EMP involved 15 kV accelerating voltage and a beam current of 20 nA. Energy-dispersive spectrometry X-ray maps collected simultaneously during EBSD acquisition on the Zeiss SEMs housed at both Macquarie Geoanalytical and ACMM provided additional information on spatially resolved chemical differences for the larger scale microstructural assessment. Garnet stoichiometry and ferric iron correction was applied after Droop (1987), whereas clinopyroxene end-member calculations follow Morimoto (1989).

Timing of mineral growth

We use the timing relationships of mineral growth relative to S_1 crystal-plastic deformation to distinguish between different crystal growth periods namely pre-D_1 igneous, syn-, and post-D_1 metamorphic. To distinguish between igneous relicts and syn-deformational growth we designated grain as neoblastic if they exhibit (i) low internal misorientation (<3°), (ii) a small grain size (<500 µm), (iii) a pronounced crystallographic preferred orientation (CPO) that matches a collective maximum and (iv) a chemical distinction that matches predicted metamorphic mineral equilibria (e.g. jadeite-rich omphacite, grossular-rich garnet and albitic plagioclase) as identified by Chapman et al. (2017). All other grains that do not fit these criteria are considered to be igneous relicts. The relicts additionally preserve their own weaker igneous CPO together with igneous microstructures (e.g. Vernon et al., 2012). Igneous relicts and neoblastic volumes were calculated via the combination of these criteria from large EBSD combined with the simultaneously acquired EDS maps within the TANGO software. Diffusive modification of the igneous relicts was not accounted for in the volume calculations due the delicate scale of these features. In generally, the method biases towards larger features, as any feature smaller than 2 times the analysis step size cannot be resolved. However, optical analysis shows that very few features are at this range (cf. Fig. 3). Furthermore, the slow igneous cooling times of the orthogneiss (*c*. 8–9 Myr) suggested by U–Pb zircon and Sm–Nd garnet ages greatly minimises these limitations (e.g. Stowell et al., 2017). Although, occurrences of late magma injections could partially obscure the structural relationships (Clarke et al., 2013), thus these areas were purposely avoided during sampling.

RESULTS

Crystallographic preferred orientations (CPO)

DOI: https://doi.org/10.2138/am-2018-6503

Crystallographic preferred orientations for omphacite and plagioclase are shown in Figures 4 and 5. Omphacite CPO is defined by a <001> point maxima contained within the foliation plane and <010> and {110} maximums forming a girdle normal to the foliation (Fig. 4). Omphacite grains with orientations distinct from this dominant CPO include porphyroclasts, coarse grain fractions (>300 μm), small euhedral grains in the matrix and mineral inclusions in garnet cores (Fig. 3). The principle axes of these grains do not coincide with the D_1 fabric trajectories (Fig. 6h), instead matching the CPO preserved in the cumulate layers (Fig. S1). The strength (*J*) of the CPO increases from 1.62 to 1.81 between low and intermediate-strain monzogabbroic gneiss, and from 4.10 to 7.17 between intermediate and high-strain monzodioritic gneiss. The change is consistent with the variation in cluster aspect ratios (Figs 2b & 4). Plagioclase CPO involves a <001> point maxima parallel to the lineation and <010> axis and (010) poles normal to the foliation (Fig. 5). The plagioclase fabric progressively strengthens from low- to intermediate-strain monzogabbroic gneiss (J = 2.94 to 5.74) and from intermediate to high-strain monzodioritic gneiss (3.14 to 6.05). Both these CPO are consistent with large data compilations of the WFO from distinct structural levels (Cyprych et al., 2017).

Microstructures and quantitative orientation analysis

According to the finite strain analysis (Fig. 2) and increasing *J*-index of plagioclase and omphacite (Figs 2–4) we describe the microstructures in the order of increasing strain. Low-strain samples as those that exhibit an average *AR* of < 2 (D = 0.45–0.54), intermediate strain samples show $2 \leq$ average $AR \leq 3$ (D = 0.74–1.19), while high-strain samples are characterized by average $AR > 3$ (D = 1.31–1.75) (Fig. 2b & 3).

Low strain: monzogabbroic gneiss (0904D)

Low-strain samples of monzogabbroic gneiss are generally coarse grained (400–1000 μm) with equant to elongate mafic grain clusters of garnet and omphacite (*AR* = 1–4). Large

DOI: https://doi.org/10.2138/am-2018-6503

omphacite (500–1000 μm) in most grain clusters has intracrystalline lattice distortions of 5–8° and is surrounded by smaller neoblasts with serrated grain boundaries and low internal deformation (Figs 3a, 6a & b). The large omphacite cores have facetted inclusions of plagioclase (Fig. 3b). Tabular omphacite grain shapes, with straight coincident faces and low apparent dihedral angles can be present in some clusters and locally intergrown with plagioclase laths in strain shadows (Fig. 3a). Grain cores of large garnet have rutile exsolution lamellae and euhedral inclusions of antiperthite feldspar and omphacite (Fig. 3c). Garnet porphyroclasts are generally substructure free, though low-angle boundaries with up to 4° of misorientation can be present (Fig. 6a). The distribution of crystallographic orientations across these garnet boundaries define rotational characteristics consistent with subgrain arrays (Fig. 6c). The plagioclase-rich matrix away from strain shadows or mafic cluster margins is generally granoblastic (200–300 μm) with texturally equilibrated triple junctions (120°) (Fig. 3d). At the margins of mafic clusters plagioclase grain size is appreciably reduced (<150 μm) and core-and-mantle microstructures are more common (Fig. 3d). The plagioclase porphyroclasts (>300 μm) exhibit undulose extinction, tapered deformation twins and irregular or sutured grain boundaries with minor bulging. The primary grain form is consistent with coincidental dihedral angles being partially overprinted during recrystallization (Fig. 3d). The porphyroclasts exhibit internal misorientation of up to 8° along the entire diameter of the grain. Surrounding the porphyroclasts are fine (<150 μm) plagioclase neoblasts (Fig. 3d).

Intermediate strain: monzogabbroic gneiss (0905B)

Gneissic layering is pronounced in intermediately strained monzogabbroic gneiss (1-3 mm: Fig. 2a). The attenuated and asymmetric mafic clusters (*AR* = 2–6) distinctively anastomose around large garnet porphyroclasts (>1000 μm) (Figs 2a & 6c). Omphacite porphyroclasts (400–1000 μm) in cluster interiors are equant to weakly elongate (*AR* = 2–3). The porphyroclasts display significant intracrystalline lattice distortion (6–15°) and variable degrees of low-angle boundary development (Figs 6e & f). Smaller omphacite grains form tails to mafic clusters (50–400 μm) and generally have less internal lattice distortion (<3°), though some exhibit low-angle boundary arrays (Figs 6e & g). All omphacite grains maintain close to 120° mutual junctions. Porphyroclastic garnet generally has limited crystal lattice distortion ranging up to 3° across the grains. Although, some grains have low-angle boundaries with up to ~8° of distortion. Facetted inclusions of substructure-free omphacite are present in the garnet cores. Coronate garnet surrounds some mafic clusters. Plagioclase exhibits less prevalent core-and-mantle microstructures than present in the lower-strain samples, although when present they occur in the centre of feldspar-rich domains (Fig. 3f). Plagioclase porphyroclasts (200–600 μm) exhibit intracrystalline lattice distortion of ~8° and have developed subgrain regions similar in size to mantled grains (50–150 μm: Fig. 3f). Outside of these domains granoblastic habit predominates the feldspar-rich matrix. Highly deformed omphacite fish (up to 700 μm) occur occasionally in the feldspar-rich matrix (Fig. 7).

Intermediate strain: monzodioritic gneiss (1203T)

Asymmetric gneissic layering and stretching is extremely pronounced in intermediate-strain monzodioritic gneiss (AR = 2–6). Elongate omphacite grain shapes are apparent for large crystals (2500 μm) that define irregular habits (Figs 3g & 8a). Large tabular omphacite grains have titano-hematite exsolution lamellae in grain cores. The omphacite porphyroclasts have significant internal lattice distortion (up to 15°), localised along curved low-angle boundaries (>2°: Figs 8b & d). The rotation of the crystallographic axes across the low-angle boundaries is consistent with them representing subgrain arrays (Fig. 8f). The size of the areas enclosed by the subgrains boundaries (~400 μm) match the sizes of equant finer grains that form the flaser tails. The grains forming the tails have low internal misorientation (<3°) or are substructure-free (Figs 8c & e). The plagioclase matrix is typically granoblastic with prevalent equilibrium triple junctions. Large plagioclase grains (>500 μm) have an abundance of tapered albite twins, which accommodate most of the lattice distortion (3°). Although, some plagioclase grains have misorientation of up to 9° accommodated along subgrain boundary arrays. Distinct intergrowths (~300 μm) of K-feldspar and plagioclase occur in the strain shadows and around the margins of elongate grain clusters. The intergrowths show similarity in the crystallographic orientations between both feldspar minerals. Plagioclase grains within the intergrowths has deformation focussed on albite twins whereas K-feldspar has intracrystalline lattice distortions of up to 5°.

High strain: monzodioritic gneiss (1203C)

Mafic grain clusters in high-strain monzodioritic gneiss are extremely stretched (*AR* of up to 7). The clusters are enveloped entirely by garnet necklaces intergrown with quartz and rutile (Fig. 3g). Garnet in these structures has vermicular to tabulate quartz inclusions commonly aligned sub-parallel to its crystal faces. Omphacite and feldspar are granoblastic and generally equant, though elongated omphacite can occur in cluster interiors (*AR* of up to 6). These elongated omphacite grains are large (500–1000 μm) and surrounded by smaller equant omphacite grains (100–400 μm: Fig. 8g). All omphacite has most internal misorientation (9°) completely localised in low-angle boundaries together with triple junctions approaching 120° (Figs 8g & i). The omphacite grains adjacent to garnet coronae are free of substructure (Figs 8l & k). The neighbouring garnet grains also generally lack any substructure. Most of the garnet grains have similar crystallographic orientations and are separated from adjacent grains by a series of low-angles boundaries (2–5°) (Fig. 8g). All the grains have crystallographic orientation relationships mimicking neighbouring omphacite (Fig. 8l). The matrix of the gneiss comprises coarse plagioclase (200–700 μm) with most preserving tapered deformation twins (Fig. 3h). The plagioclase grains have well-defined subgrain boundaries, where crystal lattice misorientation (up to 10°) is localised. Minor proportions of fine-grained plagioclase (100 μm) occur at the triple junctions of the larger grains. K-feldspar (<125 μm) occurs exclusively in an enveloping texture around garnet coronae, defining elongated and irregular shapes that are orientated within the foliation plane (Fig. 8f).

Mineral chemistry

Clinopyroxene is omphacite with jadeite contents (Jd = $100[(2Na/(2Na+Ca+Mg+Fe^{2+}))(Al_{M1}/(Al_{M1}+Fe^{3+}{}_{M1}))]$) varying throughout the felsic portions of the orthogneiss. Omphacite grain cores in low-strain monzogabbroic gneiss have lower jadeite content ($Jd_{26–27}$) than rims or neoblasts ($Jd_{30–31}$) (Fig. 7). An equivalent, though slightly more pronounced microstructural variation in jadeite content is present in intermediate-strain monzogabbroic and monzodioritic gneisses with lower absolute values; porphyroclasts have core to rim zoning of $Jd_{17–24}$, whereas grains in cluster tails are $Jd_{24–33}$ - (Fig. 9). Omphacite in high-strain samples has a tight compositional range of $Jd_{24–28}$ (Fig. S2).

Garnet end-member proportions were calculated as follows: Alm = $100Fe^{2+}/(Fe^{2+}+Mn+Mg+Ca)$, Pyp = $100Mg/(Fe^{2+}+Mn+Mg+Ca)$, Grs = $100Ca/(Fe^{2+}+Mn+Mg+Ca)$ and Sps = $100Mn/(Fe^{2+}+Mn+Mg+Ca)$. Garnet cores in monzogabbroic gneiss have the lowest grossular and highest pyrope content ($Alm_{38–39}Pyp_{42–43}Grs_{6–8}Sps_{1–2}$), enclosed by comparatively grossular enriched rims ($Alm_{38–39}Pyp_{37–40}Grs_{8–13}Sps_{1–2}$: Fig. 9). Garnet in intermediate-strain monzodioritic gneiss has core compositions of $Alm_{42–44}Pyp_{35–38}Grs_{12–14}Sps_{1–2}$ zoning to rims that are richer in grossular ($Grs_{18–25}$) but with lower pyrope ($Pyp_{30–35}$) content (Fig. 9). Garnet compositions in high-strain monzodioritic gneiss broadly match that of garnet rims in intermediate-strain samples ($Alm_{37–44}Pyp_{31–38}Grs_{12–18}Sps_{1–2}$: Fig. 9).

End-member proportions of feldspars were calculated as follows: An = 100Ca/(Ca+Na+K), Ab = 100Na/(Ca+Na+K) and Or = 100K/(Ca+Na+K). The cores of large plagioclase porphyroclasts in monzogabbroic gneiss are comparatively enriched in anorthite ($An_{34–35}Ab_{63–64}Or_{1–2}$) and enclosed by less anorthitic rims ($An_{18–22}Ab_{78–79}Or_{1}$: Fig. 9). Core compositions of plagioclase from intermediate-strain monzogabbroic gneiss are less anorthitic ($An_{26}Ab_{73}Or_{1}$) than rims ($An_{24–27}Ab_{71–73}Or_{1–3}$: Fig. 9). Similar plagioclase core–rim relationship occurs in intermediate-strain monzodioritic gneiss (core: $An_{28}Ab_{70}Or_{2}$ and rim: $An_{20–25}Ab_{73–77}Or_{1–3}$: Fig. 9). Plagioclase grain cores in high-strain monzodioritic gneiss have compositions ($An_{23–25}$) that match those of rims from intermediate-strain monzodioritic gneiss, whilst rims are more albitic ($An_{18–24}Ab_{76–79}Or_{1–3}$). Orthoclase ($An_{10–12}Ab_{1–3}Or_{87–88}$) occurs intergrown with albitic plagioclase ($An_{20}Ab_{80}$: Fig. 9).

DISCUSSION

The lower continental crust is commonly envisaged to be pervasively deformed (Bürgmann & Dresen, 2008), but features in many exposed sections are consistent with grossly heterogeneous strain (Austrheim et al., 1997; White & Clarke, 1997). In such examples, strong links can be established between regions of deformation and enhanced metamorphic transformation (Austrheim et al., 1997; White & Clarke, 1997; Jamtveit et al., 2000; Williams et al., 2014; Satsukawa et al., 2015). The Breaksea Orthogneiss is one such instance, where variations in plane-strain magnitude are strongly coupled with the extent of high-*P* Cretaceous metamorphism (Figs 1b & 2b; Clarke et al., 2013; Chapman et al., 2015, 2017). Detailed mineral chemical studies have distinguished igneous from metamorphic garnet in the orthogneiss and correlated their broad distribution in relation to strain (Clarke et al., 2013). A similar spatial distribution is apparent for the other rock-forming minerals: there is a strong association between recrystallization and metamorphic equilibration. This coincidence presents the opportunity to quantify the proportions of igneous and neoblastic materials (summarised in Fig. 10). Causal links established in two-dimensions at the grain-scale can be extended to the rock volume and the outcrop-scale based on field mapping (Figs 1–2). These data reveal the efficiency of metamorphism and its links to crystal plastic deformation that seems common in lower crustal rocks.

Quantifying igneous vs. metamorphic growth: a tool to assess metamorphic efficiency

Rock microstructure can include features that distinguish periods of mineral growth in addition to the effects of external stress. In a simple sense, differences should be observable between minerals that have largely crystallized from a silicate liquid (igneous) and those related to growth in the solid-state (metamorphic) (Vernon et al., 2012; Holness et al., 2018). Some relevant igneous microstructural features include (after Vernon et al., 2012): euhedral crystal form, facetted inclusions and dihedral angles consistent with mutual impingement (Paterson et al., 1989; Holness et al., 2006, 2018). Typically, these features are overprinted during microstructural maturation (recovery) as a consquence of prolonged heating or progressive deformation (e.g. Vernon et al., 2012; Holness et al., 2018). However, the effects of strain partitioning can leave areas that partially preserve igneous microstructure in mechanically strong grains such as pyroxene or garnet, including faceted euhedral inclusions, low apparent dihedral angles and delicate exsolution textures (Chapman et al., 2015). The additional use of crystal orientation data, lattice distortion and mineral chemistry expands the criteria that can be used to quantify the proportions of igneous *versus* metamorphic minerals.

Plastic strain in the Breaksea Orthogneiss during D_1 resulted in a well defined crystallographic fabric that developed concurrently with a general reduction in grain size (e.g. Urai et al., 1986; Yund & Tullis, 1991; Stünitz 1998). The effects of heterogenous deformation are most pronounced in domains that experienced low-strain intensity, leaving mm to cm gradations in the recrystallization of igneous grains and inefficient recovery (e.g. Svahnberg & Piazolo, 2010). Porphyroclasts of omphacite and plagioclase in low-strain domians have appreciable, but patchy, areas with lattice distortion (3–20°) that are spatially related to the development of a series of low-angle boundaries (2–10°: Figs 6i & 8d) or deformation twins (Fig. 3). Mechanically strong garnet has comparatively limited lattice distortion, and grain areas with low-angle boundary development occur where there is higher strain. Other parts of the orthogneiss that experienced higher strain have attenuated omphacite clusters and smaller grain sizes (Figs 6 & 8); the effects D_1 strain were more pervasive. In these instances, metamorphic garnet is mostly interpreted to have heterogeneously nucleated on phenocrystal clusters of garnet and omphacite, resulting in prominent necklace microstructures (Figs 6 & 8).

Microstructure in the Breaksea Orthogneiss preserves an S_1 CPO that developed during high-*P* cooling, imposed on an earlier CPO developed during crystallization of the protolith (Fig. S1; Cyprych et al., 2017). The high-*T* conditions (~850°C) inferred to have accompanied D_1 deformation and the persistence of abundant lattice distortion (Figs 6a, h & 8f) texture in garnet, pyroxene and plagioclase support an interpretation that S_1 developed via dislocation creep (after Prior et al., 2002; Brenker et al., 2002; Kruse et al., 2001). Neoblastic grains in low- and high-strain samples are crystallographically aligned with $S_{1,}$. The orientation of neoblastic omphacite and plagioclase is consistent with active creep along common slip systems: {110}[001] and (100)[001]) in omphacite (after Brenker et al., 2002), and (010)[001] in plagioclase (after Kruse et al., 2001). Although less distinct, the crystallographic alignment of garnet neoblasts is controlled by epitaxial growth on omphacite ($\{110\}_{Grt}||<001>_{Omp}$: Fig. 8l). Any deviation from the dominant S_1 CPO is thus considered to be part of an earlier igneous fabric (Figs 3, 6d & h), marked by coarse-grained porphyroclastic material (Fig 10).

The interpretation of igneous and neoblastic microstructures requires validation through the characterisation of mineral mode and chemistry, through mineral equilibria modelling (Table 2: after De Paoli et al., 2012; Chapman et al., 2017). The high-variance breakdown and removal of plagioclase to form omphacite-bearing assemblages in the Breaksea Orthogneiss is a consequence of the high-*P* cooling (Green & Ringwood, 1967; De Paoli et al., 2012; Chapman et al., 2017). Pervasively recrystallised domains have low modes of comparatively albitic plagioclase, jadeite-rich omphacite, K-feldspar, kyanite and grossular-rich garnet. The mineral assemblages correspond to $T = 850°C$ and $P = 1.8$ GPa (Fig. 9: Chapman et al., 2017). Parts of the Orthogneiss that experienced low D_1 strain have appreciably higher modes of more calcic plagioclase (~50%) than is predicted by the equilibria modelling for the inferred peak conditions (~30%, Table 2; De Paoli et al., 2012: Chapman et al., 2017). The higher mode of calcic plagioclase is consistent with that predicted for the crystallisation of a dry monzodioritic liquid at 2.0 GPa (~50%: Clarke et al*.,* 2013). In addition, porphyroclastic omphacite and garnet have chemical compositions distinct to that the metamorphic neoblasts grown during recrystallization; the former closely match the predicted phenocryst compositions (Figs 9 & 10: Clarke et al., 2013).

The combination of these petrologic criteria enable the prediction that igneous grains account for between 60 and 29% of the volume in low to intermediate-strain monzogabbroic and monzodioritic gneiss, with the remainder being neoblasts (Fig. 11). Highly strained samples comprise completely neoblastic mineral assemblages. Placing these variations in the context of observed field strain intensities (Fig. 2b) indicates that 32% of the felsic proportions Breaksea Orthogneiss can be considered to comprise igneous material. Some of this was partially modified by changes in the chemical composition of the minerals due to the effects of the high-*P* metamorphism. Heterogeneous strain conditions largely accounted for the conversion of the remainder to omphacite granulite.

Implications: Metamorphic efficiency in the lithosphere

A knowledge of phase stability at distinct P and T conditions provides the basis to extrapolate experimental results and predict lithospheric behaviour (Powell et al., 2005; Bürgmann & Dresen, 2008). In examples such as the Breaksea Orthogneiss, the efficiency of metamorphism inherently controlled the proportions of mechanical strong and weak material, and it can thus result in substantial changes to lower crustal rheology (e.g. Austrheim et al., 1997; Jackson et al., 2004; Bürgmann & Dresen, 2008). The preservation of large proportions of phenocrystal material (32% in this case study) in lower crustal rocks reflects strain partitioning at the microscopic to macroscopic scales (e.g. Williams et al., 2014). This one-third extent of metastable persistence was common, and plausibly higher, throughout much the Cretaceous Gondwana margin now exposed in Fiordland (Bradshaw et al., 1989; Daczko & Halpin, 2009; Chapman et al., 2016). It is also common in other exposures of lower crustal material (Austrheim et al., 1997; White & Clarke, 1997). It seems reasonable to assume that the effects of incomplete metamorphism are likely to be more prevalent than commonly considered for circumstances of patchy deformation, fluid-poor and short-lived metamorphic events (~10 Myr: Austrheim et al., 1997; Jamtveit et al., 2000; Štipská & Powell, 2005; Racek et al., 2008).

Quantifying the volume proportions of metastably persisting phases is therefore of practical importance in assessing the behaviour of the lower crust. Lithospheric geodynamic models should evaluate the effect of mineral mode variations beyond simplistic predictions for highly efficient metamorphism, and evaluate its influence on lithospheric dynamics. A metastable and thus mechanically strong lower crust has been considered to control exhumation dynamics and topographic expression in thickened crustal sequences (e.g. Jackson et al., 2004). In Fiordland, incomplete metamorphism in the Breaksea Orthogneiss plausibly maintained positive buoyancy in lower crust that might otherwise have been capable of foundering (Chapman et al., 2017).

CONCLUSIONS

A novel method utilising mineral orientation relationships, lattice strain and mineral chemistry collected via large-scale EBSD and EDS/WDS analysis can be used to quantify the proportion of metastable igneous minerals within a patchily deformed high-grade orthogneiss. Detailed mapping of microstructural and physiochemical relations indicates that up to 32% of the Breaksea Orthogneiss mineralogy is igneous, the remainder being metamorphic. The heterogeneous nature of the deformation facilitated the preservation of igneous mineralogy in intermediate protoliths, best developed in strain shadows to more competent material such as eclogite. The greater intensity of strain in less competent portions of the orthogneiss assisted metamorphic transformation. Metamorphic transformation at the grain scale was coincident with dynamic recrystallization, consistent with a causal role for strain in assisting reaction progress in water-poor rocks. The method highlights how inefficient metamorphism can be, even at the high-grade conditions commonly considered amenable to complete crustal transformation.

ACKNOWLEDGMENTS

TC was supported by an Australian Postgraduate Award from the University of Sydney. Logistical and analytical funding was provided by the School of Geosciences, the University of Sydney (GLC) and through the ARC Discovery Project and Future Fellowship (DP120102060 to SP and NRD; FT1101100070 to SP). D. Cyprych and P. Trimby are thanked for help with data collection, and the Department of Conservation in Te Anau for permission to visit and sample localities at Breaksea Sound, Fiordland National Park. The authors acknowledge the facilities, scientific and technical assistance of the Australian Microscopy & Microanalysis Research Facility at the Australian Centre for Microscopy & Microanalysis at the University of Sydney. The manuscript was improved after reviews from A. Indares and editorial handling of P. Cordier. This is contribution XX from the ARC Centre of Excellence for Core to Crust Fluid Systems (http://www.CCFS.mq.edu.au) and XX from GEMOC (http://www.GEMOC.mq.edu.au). The analytical data were obtained using instrumentation funded by DEST Systemic Infrastructure Grants, ARC LIEF, NCRIS, industry partners and Macquarie University.

REFERENCES CITED

Allibone, A.H., Jongens, R., Turnbull, I.M., Milan, L.A., Daczko, N.R., De Paoli, M.C., & Tulloch, A.J. (2009a). Plutonic rocks of western Fiordland, New Zealand: field relations, geochemistry, correlation and nomenclature. New Zealand Journal of Geology and Geophysics, 52, 379–415.

Austrheim, H., Erambert, M., & Engvik, A.K. (1997). Processing of crust in the root of the Caledonian contientnal collision zone: the role of eclogitization. Tectonophysics, 273, 129–153.

Betka, P.M., & Klepeis, K.A. (2013). Three-stage evolution of lower crustal gneiss domes at Breaksea Entrance, Fiordland, New Zealand. Tectonics, 32, 1084–1106.

Bradshaw, J.Y. (1989). Origin and metamorphic history of an Early Cretaceous polybaric granulite terrain, Fiordland, southwest New Zealand. Contributions to Mineralogy and Petrology, 103, 346–360.

Bunge, H.J. (1982). Texture analysis in materials science. Butterworths, London.

Bürgmann, R., & Dresen, G. (2008). Rheology of the lower crust and upper mantle: evidence from rock mechanics, geodesy, and field observations. Annual Reviews of Earth and Planetary Sciences, 36, 531–567.

Brenker, F.E., Prior, D.J., & Müller, W.F. (2002). Cation ordering in omphacite and effect on deformation mechanism and lattice preferred orientation (LPO). Journal of Structural Geology, 24, 1991–2005.

Chapman, T., Clarke, G.L., Daczko, N.R., Piazolo, S., & Rajkumar, A. (2015).

DOI: https://doi.org/10.2138/am-2018-6503

Orthopyroxene–omphacite- and garnet–omphacite-bearing magmatic assemblages, Breaksea Orthogneiss, New Zealand: oxidation state controlled by high-*P* oxide fractionation. Lithos, 216–217, 1–16.

Chapman, T., Clarke, G.L., & Daczko, N.R. (2016). Crustal differentiation in a thickened arc — evaluating depth dependencies. Journal of Petrology, 57, 595–620.

Chapman, T., Clarke, G.L., Piazolo, S., & Daczko, N.R. (2017). Evaluating the importance of metamorphism in the foundering of continental crust. Scientific Reports 7, DOI:10.1038/s41598-017-13221-6.

Clarke, G.L., Daczko, N.R., & Miescher, D. (2013). Identifying relict igneous garnet and clinopyroxene in eclogite and granulite, Breaksea Orthogneiss, New Zealand. Journal of Petrology, 54, 1921–1938.

Cyprych, D., Piazolo, S., & Almqvist, B.S.G. (2017). Seismic anisotropy from compositional banding in granulites from the deep magmatic arc of Fiordland, New Zealand. Earth and Planetary Science Letters, 477, 156–167.

Daczko, N.R., & Halpin, J.A. (2009). Evidence for melt migration enhancing recrystallization of metastable assemblages in mafic lower crust, Fiordland, New Zealand. Journal of Metamorphic Geology, 27, 167–185.

De Paoli, M.C., Clarke, G.L., Klepeis, K.A., Allibone, A.H., & Turnbull, I.M. (2009). The eclogite–granulite transition: mafic and intermediate assemblages at Breaksea Sound, New Zealand. Journal of Petrology, 50, 2307–2343.

De Paoli, M.C., Clarke, G.L., & Daczko, N.R. (2012). Mineral equilibria modeling of the granulite–eclogite transition: effects of whole-rock composition on metamorphic facies type-assemblages. Journal of Petrology, 53, 949–970.

This is a preprint, the final version is subject to change, of the American Mineralogist (MSA)
Cite as Authors (Year) Title. American Mineralogist, in press.
DOI: https://doi.org/10.2138/am-2018-6503

Droop, G.T.R. (1987). A general equation for estimating Fe^{3+} concentrations in ferromagnesian silicates and oxides from microprobe analyses, using stoichiometric criteria. Mineralogical Magazine, 51, 431–435.

Flinn, D. (1965). On the symmetry principle and the deformation ellipsoid. Geological Magazine, 102, 36–45.

Green, D.H., & Ringwood, A.E. (1967). An experimental investigation of the gabbro to eclogite transformation and its petrological applications. Geochimica et Cosmochimica Acta, 31, 767–833.

Holness, M.B. (2006). Melt-solid dihedral angles of common minerals in natural rocks. Journal of Petrology, 47, 791–800.

Holness, M.B., Vukmanovic, Z., & Mariani, E. (2017). Assessing the role of compaction in the formation of adcumulates: a microstructural perspective. Journal of Petrology, 58, 643–674.

Holness, M.B., Clemens, J.D. & Vernon, R. H. (2018). How deceptive are microstructures in granitic rocks? Answers from integrated physical theoru, phase equilibrium, and direct observations. Contributions to Mineralogy and Petrology, 173, 2–18.

Jackson, J.A., Austrheim, H., McKenzie, D., & Priestley, K. (2004). Metastability, mechanical strength, and the support of mountain belts. Geology, 32, 625–628.

Jamtveit, B., Austrheim, H., & Malthe-Sørenssen, A. (2000). Accelerated hydration of the Earth's deep crust induced by stress perturbations. Nature, 408, 75–78.

Klepeis, K.A., King, D., De Paoli, M., Clarke, G.L. & Gehrels, G. (2007). Interaction of strong lower and weak middle crust during lithospheric extension in western New Zealand. Tectonics, 26, 1–27.

Klepeis, K.A., Schwartz, J., Stowell, H., & Tulloch, A.J. (2016). Gneiss domes, vertical and horizontal mass transfer, and the initiation of extension in the hot lower-crustal root of a continental arc, Fiordland, New Zealand. Lithosphere, 8, 116–140.

Kruse, R., Stünitz, H., & Kunze, K. (2001). Dynamic recrystallization processes in plagioclase porphyroclasts. Journal of Structural Geology, 23, 1111–1115.

Marmo, B.A., Clarke, G.L., & Powell, R. (2002). Fractionation of bulk rock composition due to porphyroblast growth: effects of eclogite facies mineral equilibria, Pam Peninsula, New Caledonia. Journal of Metamorphic Geology, 20, 151–165.

Mainprice, D., Hielscher, R., & Schaeben, H. (2011). Calculating anisotropic physical properties from texture data using the MTEX open-source package. In Prior, D. J., Rutter, E. H., Tatham, D. J. (Eds.) Deformation mechanisms, rheology and tectonics: microstructures, mechanics and anisotropy. Geological Society of London Special Publication 360, 175–192.

Milan, L.A., Daczko, N.R., Clarke, G.L., & Allibone, A.H. (2016). Complexity of *in situ* U Pb–Hf isotope systematics during arc magma genesis at the roots of a Cretaceous arc, Fiordland, New Zealand. Lithos, 264, 296–314.

Milan, L.A., Daczko, N.R. & Clarke, G.L. (2017). Cordillera Zealandia: A Mesozoic arc flare-up on the palaeo-Pacific Gondwana margin. Scientific Reports, doi:10.1038/s41598-017-00347-w.

Miranda, E.A., & Klepeis, K.A. (2016). The interplay and effects of deformation and crystallized melt on the rheology of the lower continental crust, Fiordland, New Zealand. Journal of Structural Geology, 93, 91–105.

Morimoto, N. (1989). Nomenclature of pyroxenes. Canadian Mineralogist, 27, 143–156.

Paterson, S.R., Vernon, R.H., & Tobisch, O.T. (1989). A review of criteria for the identification of magmatic and tectonic foliations in granitoids. Journal of Structural Geology, 11, 349–363.

Piazolo, S., Bestmann, M., Prior, D.J., & Spiers, C.J. (2006). Temperature dependent grain boundary migration in deformed-then-annealed material: observations from experimentally deformed synthetic rocksalt. Tectonophysics, 427, 55–71.

Piazolo, S., La Fontaine, A., Trimby, P., Harley, S., Yang, L., Armstrong, R., & Cairney, J. (2016). Deformation-induced trace element redistribution in zircon revealed using atom probe tomography. Nature Communications, DOI: 10.1038/ncomms10490.

Powell, R. Guiraud, M., & White, R.W. (2005). Truth and beauty in metamorphic phase equilibria: conjugate variables and phase diagrams. The Canadian Mineralogist, 43, 21–33.

Prior, D.J., Boyle, A.P., Brenker, F., Cheadle, M.C., Day, A., Lopez, G., Peruzzo, L., Potts, G.J., Reddy, S., Spiess, R., Timms, N.E., Trimby, P., Wheeler, J., & Zetterström, L. (1999). The application of electron backscatter diffraction and orientation contrast imaging in the SEM to textural problems in rocks. American Mineralogist, 84, 1741–1759.

Prior, D.J., Wheeler, J., Peruzzo, L., Spiess, R., & Storey, C. (2002). Some garnet microstructures: an illustration of the potential of orientation maps and misorientation analysis in microstructural studies. Journal of Structural Geology, 24, 999–1011.

Racek, M., Štípská, P,. & Powell, R. (2008). Garnet–clinopyroxene intermediate granulites in the St. Leonhard massif of the Bohemian Massif: ultrahigh-temperature metamorphism at high pressure or not? Journal of Metamorphic Geology, 26, 253–271.

Satsukawa, T., Piazolo, S., González-Jiménez, J.M., Colás, V., Griffin, W.L., O'Reilly, S.Y., Gervilla, F., Fanlo, I., & Kerestedjian, T.N. (2015). Fluid-present deformation aids chemical modification of chromite: insights from chromites from Golyamo Kamenyane, SE Bulgaria. Lithos, 228–229, 78–89.

Smith, J.R., Piazolo, S., Daczko, N.R., & Evans, L. (2015). The effect of pre-tectonic reaction and annealing extent on behaviour during subsequent deformation: Insights from paired shear zones in the lower crust of Fiordland, New Zealand. Journal of Metamorphic Geology, 33, 557–577.

Štípská, P., & Powell, R. (2005). Does ternary feldspar constrain the metamorphic conditions of high-grade meta-igneous rocks? Evidence from orthopyroxene granulites, Bohemian Massif. Journal of Metamorphic Geology, 23, 627–647.

Stowell, H.H., Schwartz, J.J., Klepeis, K.A., Hout, C., Tulloch, A.J., & Koenig, A. (2017). Sm-Nd garnet ages for granulite and eclogite in the Breaksea Orthogneiss and widespread granulite facies metamorphism of the lower crust, Fiordland magmatic arc, New Zealand. Lithosphere, DOI: 10.1130/L662.1.

Stünitz, H. (1998). Syndeformational recrystallization — dynamic or compositionally induced? Contributions to Mineralogy and Petrology, 131, 219–236.

Stüwe, K. (1997). Effective bulk composition changes due to cooling: a model predicting complexities in retrograde reaction textures. Contributions to Mineralogy and Petrology, 129, 43–52.

Svahnberg, H., & Piazolo, S., 2010. The initiation of strain localization in plagioclase-rich rocks: insights from detailed microstructural analyses. Journal of Structural Geology, 32, 1404–1416.

Urai, J.L., Means, W.D., & Lister, G.S. (1986). Dynamic recrystallization of minerals. In Hobbs, B.E., Heard, H.C. (Eds.). Mineral and rock deformation (laboratory studies). Geophysical monograph of the American Geophysical Union, 36, pp. 161–200.

White, R.W., & Clarke, G.L. (1997). The role of deformation in aiding recrystallization: an example from a high-pressure shear zone, Central Australia. Journal of Petrology, 38, 1307–1329.

Williams, M.L., Dumond, G., Mahan, K., Regan, S., & Holland, M. (2014). Garnet-forming reactions in felsic orthogneiss: implications for densification and strengthening the lower crust. Earth and Planetary Science Letters, 405, 207–219.

Vernon, R.H. (2004). A practical guide to rock microstructure. Cambridge University Press, Cambridge, UK.

Vernon, R.H., White, R.W., & Clarke, G.L. (2008). False metamorphic events inferred from misinterpretation of microstructural evidence and *P–T* data. Journal of Metamorphic Geology*, 26*, 437–449.

Vernon, R.H & Paterson, S.R. (2008). How extensive are subsolidus grain-sahpe changes in cooling granites? Lithos, 105, 42–50.

Vernon, R.H., Collins, W.J., & Cook, N.D.J. (2012). Metamorphism and deformation of mafic and felsic rocks in a magma transfer zone, Stewart Island, New Zealand. Journal of Metamorphic Geology, 30, 473–488.

Yund, R.A., & Tullis, J. (1991). Compositional changes of minerals associated with dynamic recrystallization. Contributions to Mineralogy and Petrology, 108, 346–355.

Figure captions

Figure 1a Simplified geological map of the Breaksea Sound area between northern Resolution Island and Coal River. Circles show sample locations and inset shows the structure at Breaksea Tops. Structural relationships in red and foliation trajectories are from

Klepeis et al. (2016). **b** Detailed outcrop relationships showing distribution of strain surrounding an eclogite pod, near sample location 0904D.

Figure 2a Hand specimens of the monzogabbroic to monzodioritic gneiss showing typical variation in mineral assemblages and strain. Boxes represent approximate locations of studied samples, MG = monzogabbroic and MD = monzodioritic. **b** Flinn diagram of mafic cluster shapes. Values of *D* represent the intensity of strain defined as the distance from the origin, and *K* the slope defines the type of strain symmetry.

Figure 3a Mafic grain cluster in low-strain monzogabbroic gneiss comprising intergrown igneous garnet and omphacite (see Fig. 6). Omphacite grains in places have coincidental crystal form. **b** Deformed omphacite phenocryst with facetted and euhedral plagioclase inclusions (arrow). **c** Large Igneous garnet with crystallographically aligned rutile exsolution (arrow) and facetted plagioclase inclusion displaying a perfect growth twin (arrow). **d** Large interlocking plagioclase grains in low-strain monzogabbroic gneiss. Note the low apparent dihedral angles, undulose extinction, sutured grain boundaries (arrows) and small neoblasts. **e** Large omphacite porphyroclasts in intermediate-strain monzodioritic gneiss, with internal titano-hematite exsolution. **f** Variably recrystallised feldspar-rich matrix in an intermediately-strained monzogabbroic gneiss. Large plagioclase porphyroclasts are present in the top right, neoblasts occur closer to the cluster margins. **g** Attenuated mafic grain clusters in high-strain monzodioritic gneiss, surrounded by necklaces of neoblastic garnet, quartz, rutile and K-feldspar. **h** Granoblastic feldspar-rich matrix from high-strain monzodioritic gneiss. Grain triple junctions are close to 120° (arrow).

Figure 4 Lower hemisphere pole figures displaying omphacite CPO (one point per grain) for the studied strain gradients. *J* = texture index, MUD refers to maximum mean uniform distribution values, *n* is the number of grains and *AR* (X/Y) is the mean aspect ratio of grain cluster from the samples. Int. = intermediate. Top to the right sense of shear. Maps accompanying the pole figures are shown in Figure 9.

Figure 5 Lower hemisphere pole figures displaying plagioclase (one point per grain) CPO for the studied strain gradients. *J* = texture index, max refers to mean uniform distribution values and *n* is the number of grains. Maps accompanying the pole figures are shown in Figure 9.

Figure 6 Microstructures from two samples of monzogabbroic gneiss. **a** EBSD mineral map of grain cluster in low-strain monzogabbroic gneiss (0904D: Fig. 3a), low angle (2–10°) subgrain boundaries (sgb) shown in yellow and grain boundaries (>10°: gb) in black. Black arrows point to small neoblasts and white arrows to porphyroclasts. **b** Crystal misorientation profile showing gradual lattice distortion in porphyroclast marked in **a**. **c** Misorientation axis distribution (crystal coordinate reference frame) across a low-angle boundary (2–10°) in garnet shown in **a**. **d** Lower hemisphere pole figures utilising the XYZ structural reference frame (one point per grain) of omphacite grains in the cluster shown in **a**. MUD refers to the maximum mean uniform distribution and *n* is the number of grains. **e** Orientation contrast forescatter image of omphacite grain cluster in the intermediate-strain monzogabbroic gneiss (0905B). **f–g** Crystallographic misorientation from specific reference point (red cross) in porphyroclast (rainbow; **f**) and neoblast (green; **g**). **h** Lower hemisphere pole figures of omphacite grains across the microstructure (shown by circle and squares in **e**). Rotation from porphyroclast orientations to those of grains in the tails is apparent. **i–j** Crystal misorientation profiles showing gradual lattice distortion in porphyroclast (**f**) and neoblast (**g**).

Figure 7 Crystallographic misorientation from specific reference point (red cross: **a**) and associated profile (white line) showing lattice distortion and subgrain orientation and mineral jadeite content in omphacite fish from the intermediate-strain monzodioritic gneiss (**b**).

Figure 8 Microstructures from two samples of monzodioritic gneiss. **a** Backscatter electron image of grain cluster in intermediate strain monzodioritic gneiss (1203T: Fig. 3e). **b–e**

DOI: https://doi.org/10.2138/am-2018-6503

Crystallographic misorientation from specific reference point (red cross) and associated profiles showing gradual lattice distortion and subgrain orientation in omphacite porphyroclast (rainbow; **b** & **d**) and neoblast (green; **c** & **e**). **f** Misorientation axis distribution (crystal coordinate reference frame) across a low-angle boundary (2–10°) shown in **b**. **g** Backscatter electron image of omphacite grain cluster in high-strain monzodioritic gneiss (1203C: Fig. 3g). **h–k** Crystallographic misorientation from specific reference point (red cross) and associated profiles showing gradual lattice distortion and subgrain orientation in omphacite porphyroclast (rainbow; **h** & **j**) and neoblast (green; **i** & **k**). **l** Pole figures of adjacent omphacite and garnet grains (red & black dots in **a**).

Figure 9 Composite ternary plot of feldspar, garnet and clinopyroxene microprobe analyses, respectively with apices Ab–Or–An, Jd–Aeg–Q and Pyp–Alm–Grs+Sps for strain proportions of monzogabbro (MG) and monzodiorite (MD) in the Breaksea Orthogneiss.

Figure 10 Schematic of the microstructural and chemical distinctions across microstructures. Chemical variation diagram of plagioclase anorthite content (An), garnet grossular content (Grs) and omphacite jadeite (Jd) content across the profile, arrows represent within sample variability that changes across igneous and neoblasts (arrow head), subordinate to overall changes across the strain gradient. Simple pole figure displays igneous omphacite CPO.

Figure 11 Large-scale EBSD maps of (**a–b**) low- and intermediate-strain monzogabbroic and (**c–d**) intermediate- and high-strain monzodioritic gneisses. Highlighted grains represent material interpreted as igneous relicts based on location, grain size and internal deformation, transparent grains are neoblasts.

Supplementary Figure 1 Lower hemisphere pole figures displaying clinopyroxene CPO (one point per grain) for cumulate clinopyroxenite and eclogite in the Breaksea Orthogneiss. MUD refers to maximum mean uniform distribution values and *n* is the number of grains.

Supplementary Figure 2 WDS X-ray maps from intermediate-strain monzodioritic gneiss (0905B) **a** phase map with grain boundaries in black and subgrain boundaries in yellow of Al (**b**), Ca (**c**) and Na (**d**) proportions in omphacite, Ca (**e**) and Mg (**f**) proportions in garnet and Ca proportions in plagioclase (**g**). Zoning in omphacite overprints all grains. Garnet zoning is asymmetrical towards mineral boundaries with plagioclase. Plagioclase albite content is zoned towards omphacite. Image size is *c*. 2 x 2 cm.

Table 1 Summary of the tectonometamorphic history of the Breaksea Orthogneiss.

T (Ma)	*P* (GPa)	*T* (°C)	*D*	assemblages	tectonometamorphic event	ref.
124–115	1.8	950–1200	Ign	Grt–Omp–Pl–Opx	Pluton emplacement, layering and accumulation	1, 2, 3, 4, 8
124–115	1.8	800–950	D_1	Grt–Omp–Pl	Metamorphism and S_1–L_1 fabric	1, 2, 5, 6, 8
115–105	10–1.4	650–750	Post-D_1	Di–Ab and Hb–Pl	Near-isothermal decompression, decimetre dome formation	1, 5, 6
105–90	0.9–1.4	650–750	D_2	Hb–Pl	Extensional shear zones, collapse and foundering	1, 6, 7, 8

1 Chapman et al. (2017); 2 Clarke et al. (2013); 3 Chapman et al. (2015); 4 Milan et al. (2016); 5 De Paoli et al. (2009); 6 Klepeis et al. 2016); 7 Klepeis et al. (2007); 8 Stowell et al. (2017)

Table 2 Observed mineral modes across the two strain profiles and predicted modes from mineral equilibria modelling of a monzodiorite and monzogabbro at *T* = 850°C and *P* = 1.8 GPa after Chapman et al. (2017).

	monzogabbro			monzodiorite		
	low-strain 0904D	intermediate-strain 0905B	modelled	intermediate-strain 1203T	high-strain 1203C	modelled
grt_{Ig}	24	16		3		
grt_N		4	28		24	25
omp	25	21	32	24	24	29
pl	45	49	22	60	31	27
kfs	0.5	3.5	0.5	10	9	2
ky	1	2	6	0.5	3	3
rt	1	2	1	1	1	1
qtz	1.5	0.5	3.5	1	6	6
ap	0.5	1	na	0.5	1	na
hbl	1.5	1			1	
mu			5*			7*

*models overestimate mu on account of small proportions of H_2O, partially reducing kfs mode

Table 3 Representative electron microprobe analysis of minerals from the two strain profiles.

low-strain MG 0904D	omp_{Ig} core	omp_{Ig} rim	grt_{Ig} core	grt_{Ig} rim	pl_{Ig}	pl_{N}
SiO_2	51.69	52.25	39.44	39.46	63.08	63.98
TiO_2	0.54	0.49	0.06	0.06	0.00	0.00
Al_2O_3	11.27	11.47	21.34	21.23	22.74	22.57
Cr_2O_3	0.00	0.00	0.00	0.00	0.00	0.00
FeO	7.51	7.14	21.33	21.30	0.08	0.06
MnO	0.00	0.00	0.49	0.53	0.00	0.00
MgO	8.43	8.10	11.21	11.23	0.00	0.00
CaO	16.14	15.40	6.47	6.66	3.87	3.86
Na_2O	4.91	5.40	0.05	0.04	9.30	9.47
K_2O	0.00	0.00	0.00	0.00	0.66	0.43
Total	100.49	100.25	100.39	100.51	99.73	100.37

Table 3 cont.

int.-strain MG 0905B	omp_{Ig}	omp_{N}	grt_{Ig} core	grt_{Ig} rim	pl_{Ig}	pl_{N}
SiO_2	49.92	61.07	38.79	38.83	62.28	61.76
TiO_2	1.00	0.00	0.08	0.07	0.00	0.00
Al_2O_3	9.42	24.38	21.84	21.71	23.52	23.74
Cr_2O_3	0.00	0.00	0.00	0.00	0.00	0.00
FeO	8.65	0.34	21.27	20.56	0.10	0.09
MnO	0.06	0.00	0.54	0.41	0.00	0.00
MgO	9.22	0.07	9.91	9.16	0.00	0.00
CaO	18.21	6.40	7.91	9.40	5.20	5.24
Na_2O	3.50	7.80	0.04	0.03	8.42	8.35
K_2O	0.00	0.34	0.00	0.00	0.49	0.70
Total	99.98	100.40	100.46	100.17	100.01	99.88

Table 3 cont.

Int.-strain MD 1203T	omp_{Ig}	omp_{N}	grt_{Ig} core	grt_{Ig} rim	pl_{Ig}	pl_{N}
SiO_2	51.19	49.99	39.35	39.65	61.00	61.42
TiO_2	0.32	0.58	0.04	0.09	0.00	0.00
Al_2O_3	6.07	13.06	22.11	22.20	23.82	24.04
Cr_2O_3	0.01	0.00	-0.01	0.02	0.00	0.00
FeO	8.56	8.61	21.38	21.87	0.07	0.05
MnO	0.06	0.05	0.66	0.63	0.00	0.00
MgO	11.36	7.32	9.83	10.17	0.00	0.00
CaO	19.90	15.49	7.38	6.29	4.89	4.98
Na_2O	2.35	4.94	0.03	0.01	8.56	8.43
K_2O	0.00	0.01	0.01	0.00	0.52	0.50
Total	100.08	100.28	100.92	101.03	98.95	99.49

Table 3 cont.

high-strain MD 1203C	omp_{N} core	omp_{N} rim	grt_{N} core	grt_{N} rim	pl_{RN} core	pl_{N} rim
SiO_2	50.95	52.04	38.74	38.77	62.02	62.45
TiO_2	0.74	0.63	0.05	0.03	0.00	0.00
Al_2O_3	10.28	10.04	21.78	21.96	23.34	23.38
Cr_2O_3	0.05	0.00	0.00	0.00	0.00	0.00
FeO	8.26	8.00	21.70	21.19	0.00	0.00
MnO	0.04	0.00	0.57	0.45	0.00	0.00
MgO	8.46	8.51	10.11	9.51	0.00	0.00
CaO	16.67	16.36	6.83	8.24	5.06	5.02
Na_2O	4.27	4.55	0.02	0.00	8.60	8.89
K_2O	0.00	0.00	0.00	0.00	0.48	0.47
Total	99.72	100.13	99.80	100.15	99.50	100.21

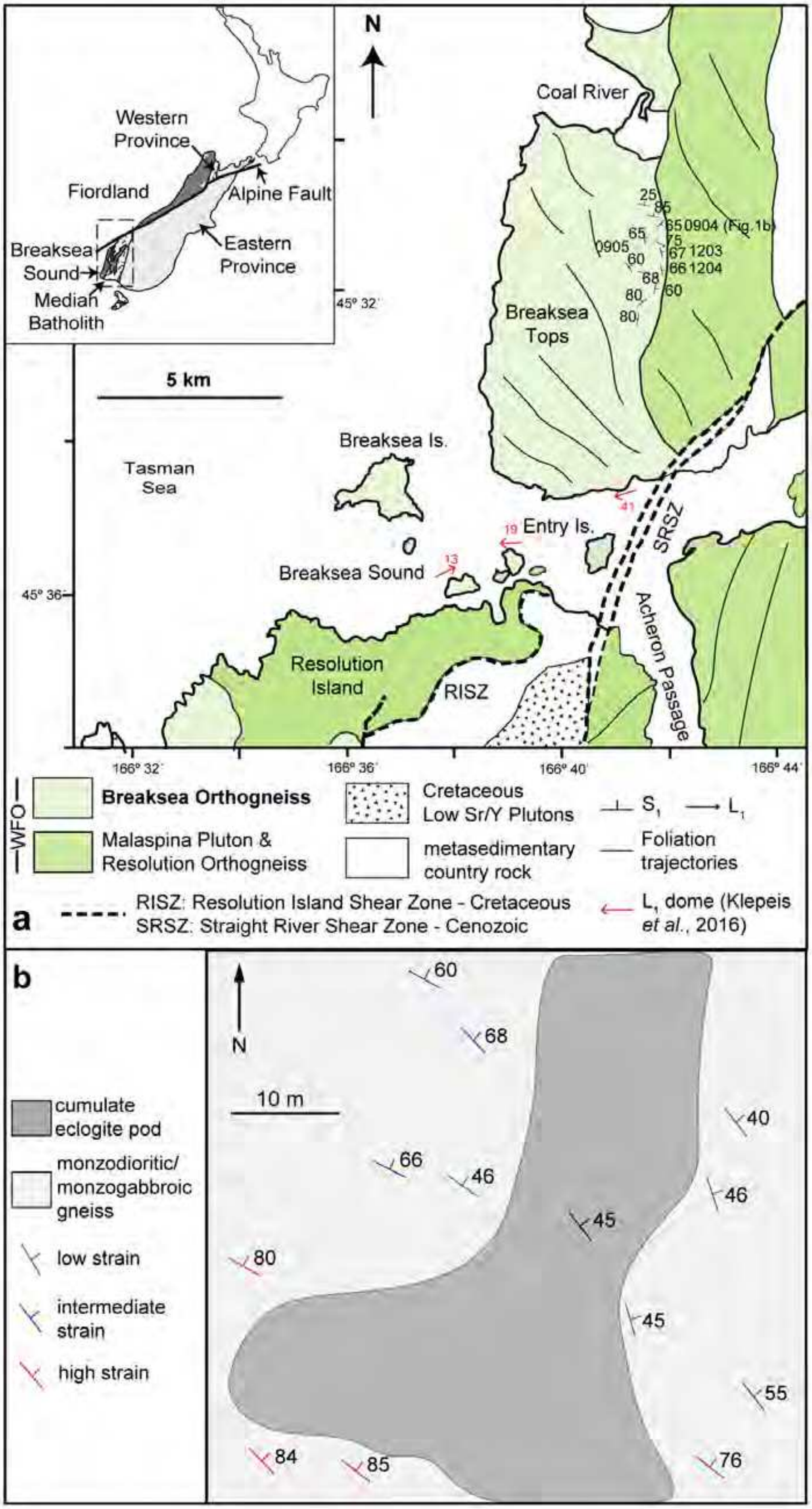

Chapman et al. Figure 1

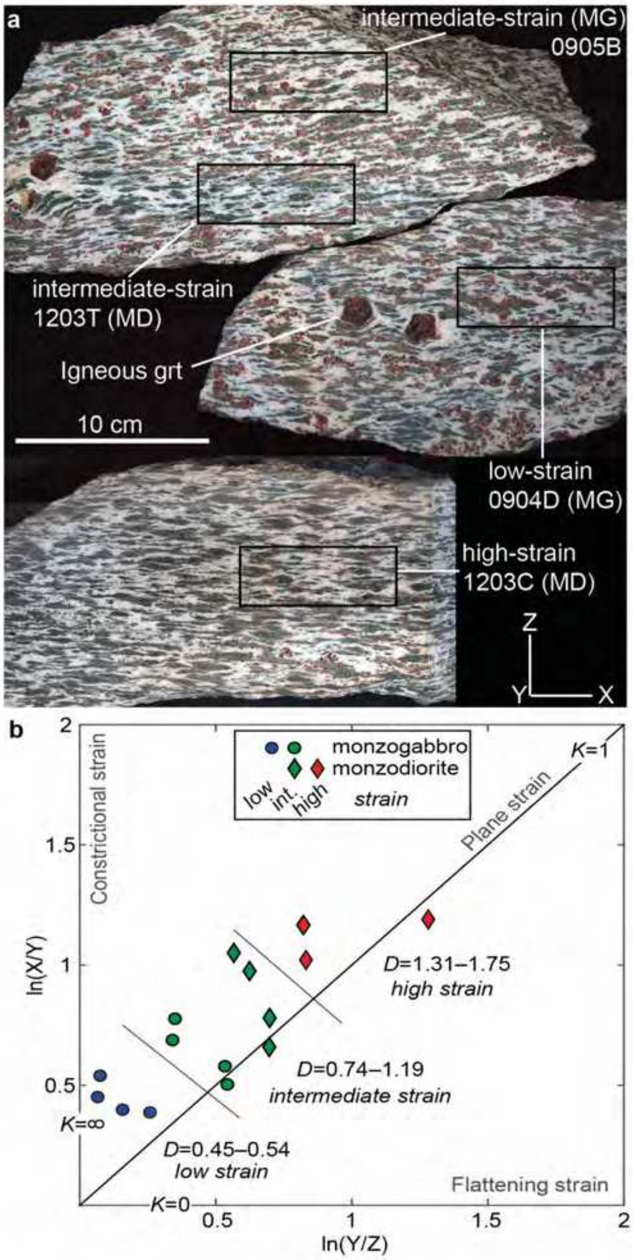

Chapman et al. Figure 2

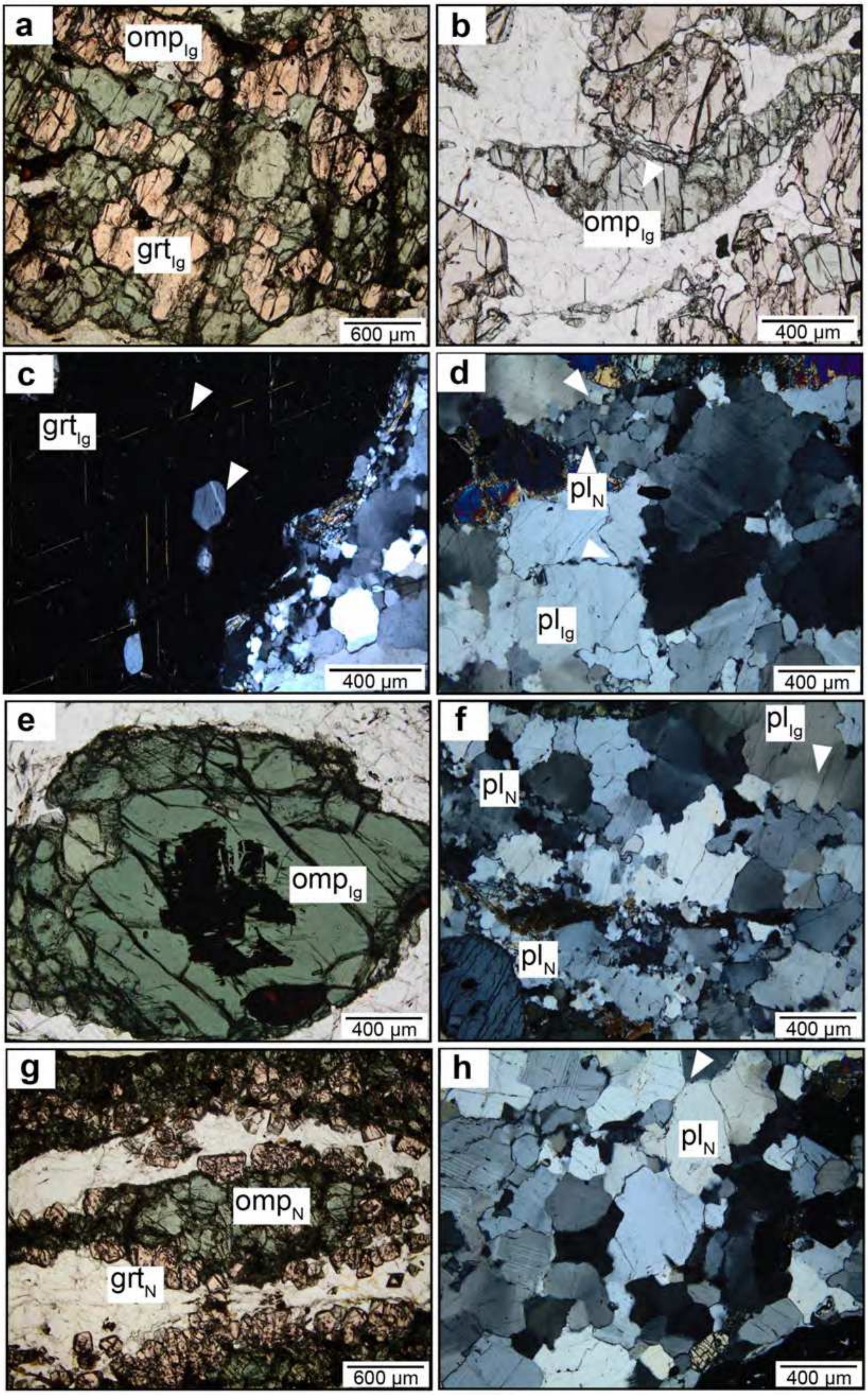

Chapman et al. Figure 3

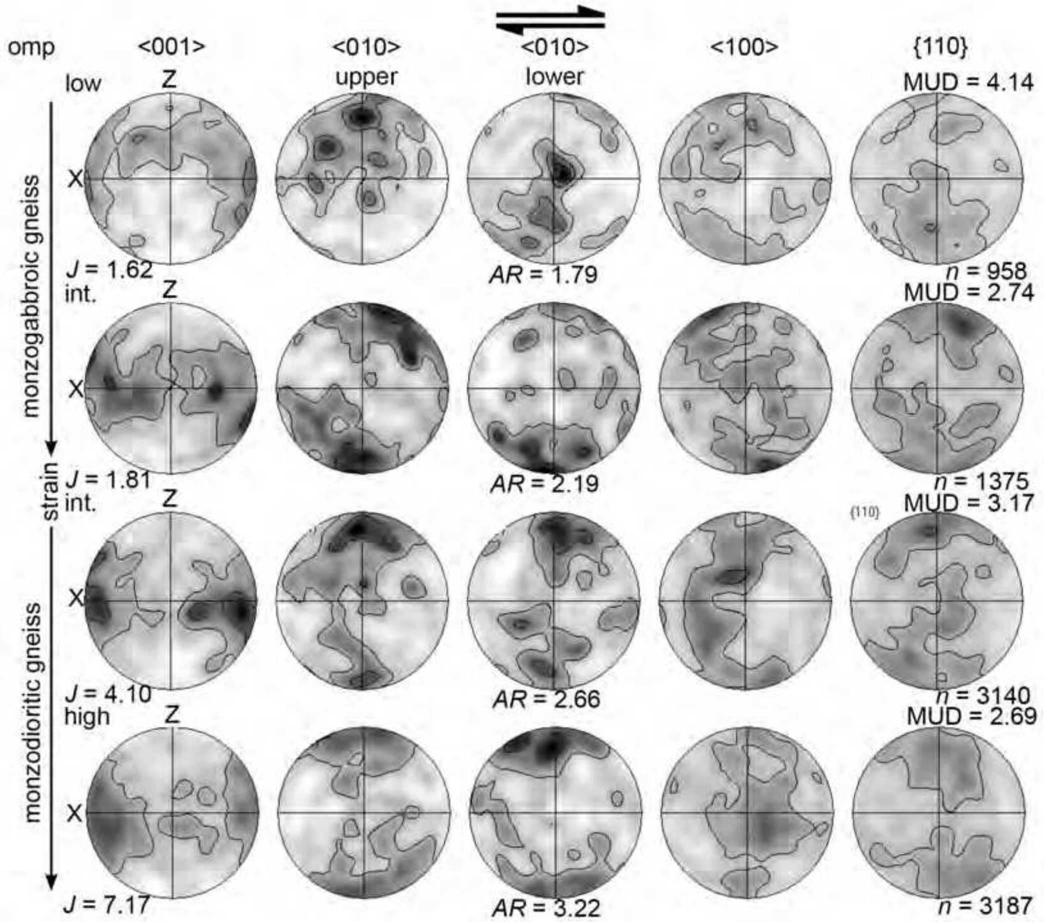

Chapman et al. Figure 4

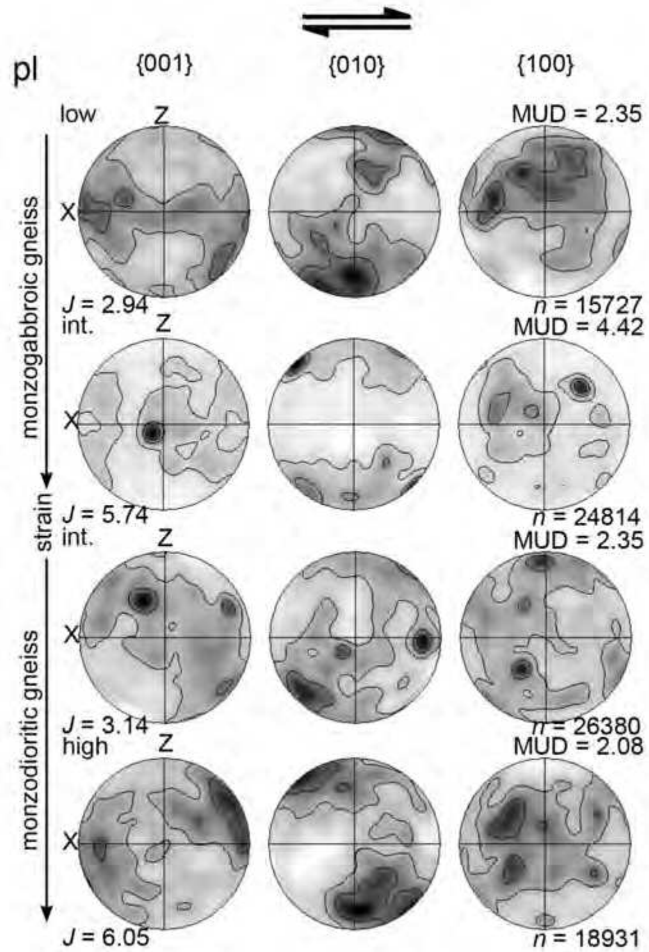

Chapman et al. Figure 5

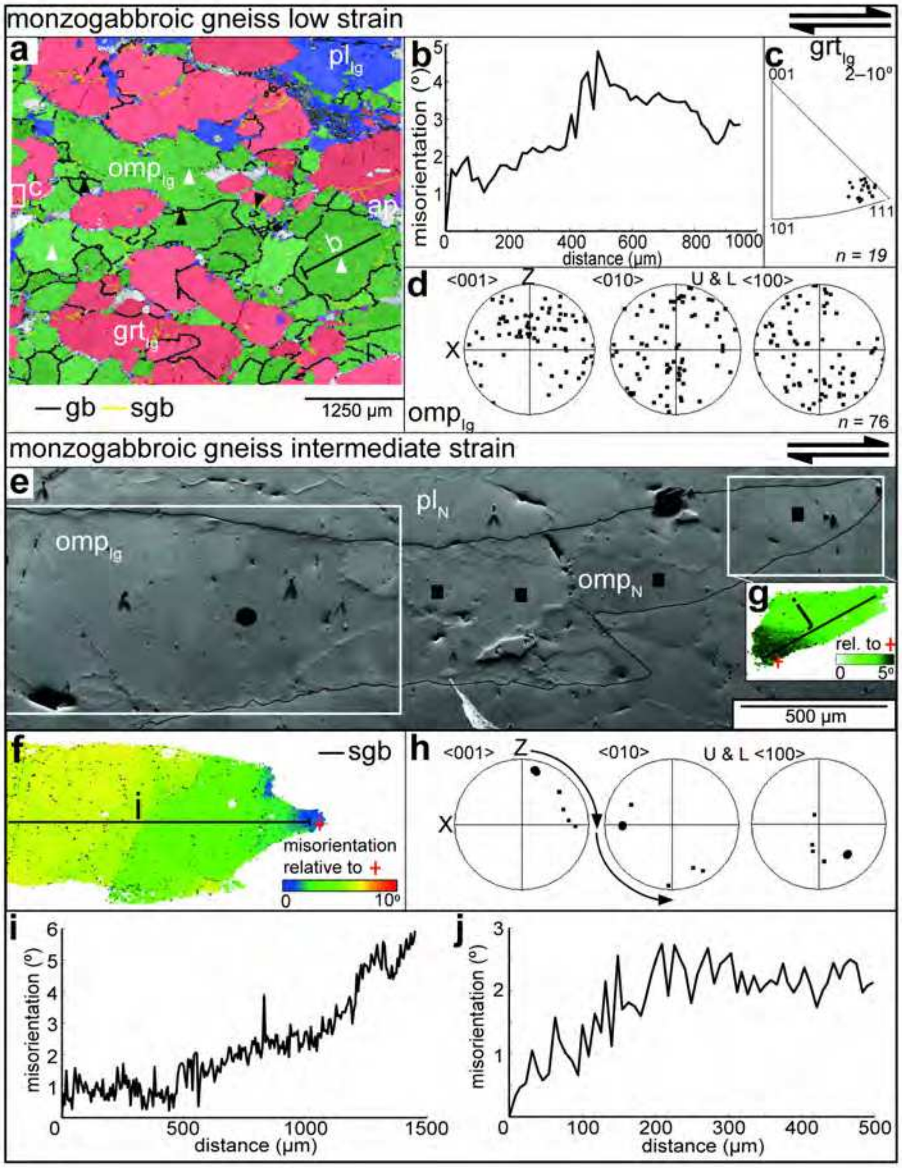

Chapman et al. Figure 6

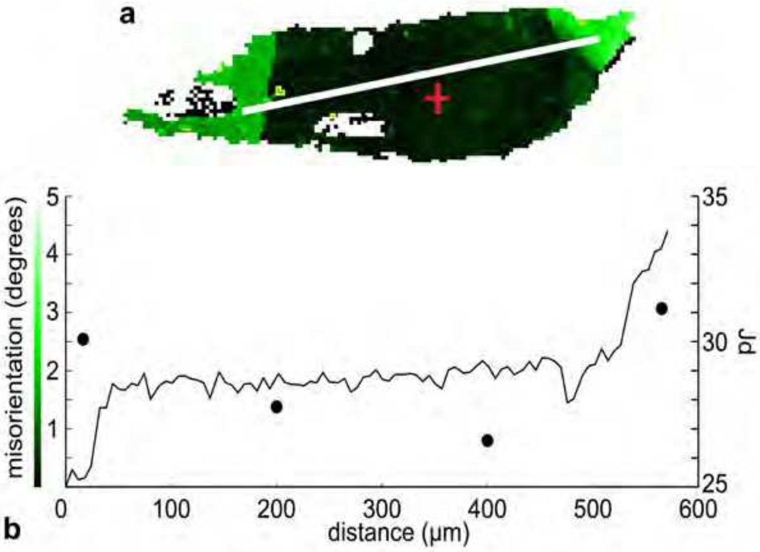

Chapman et al. Figure 7

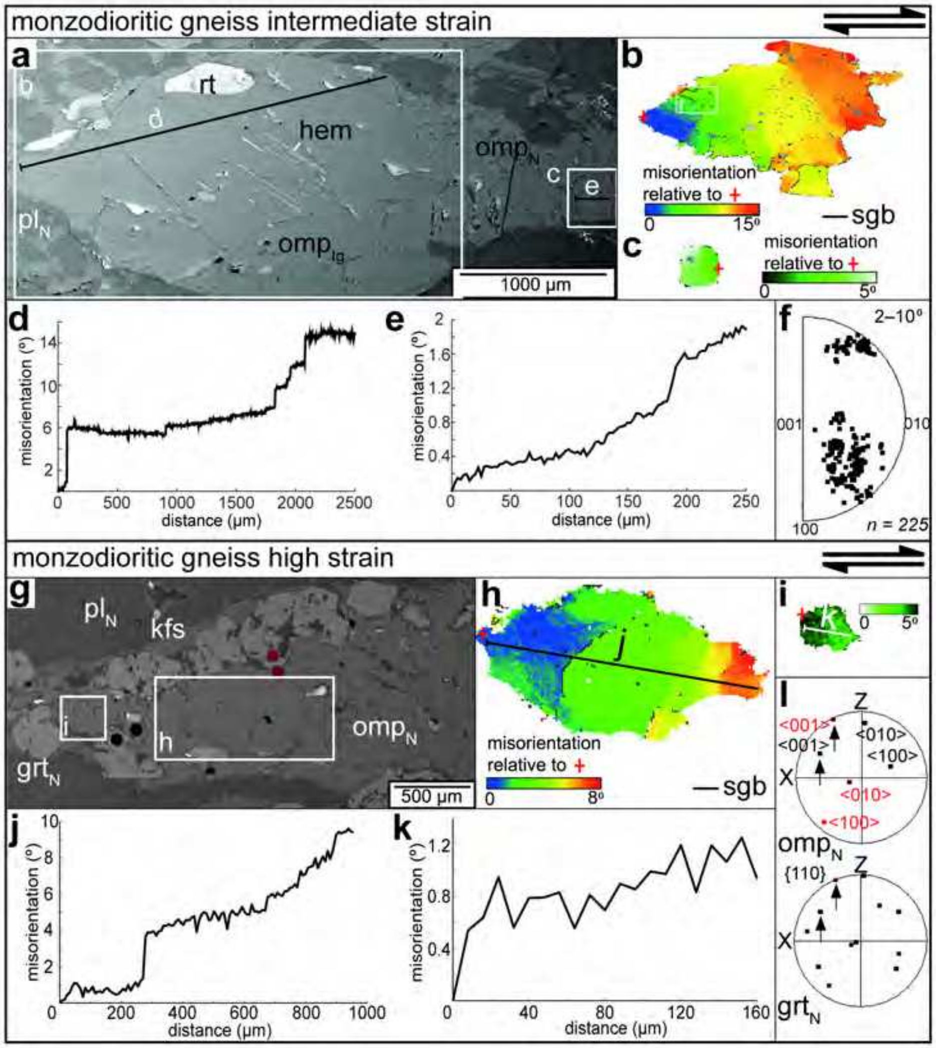

Chapman et al. Figure 8

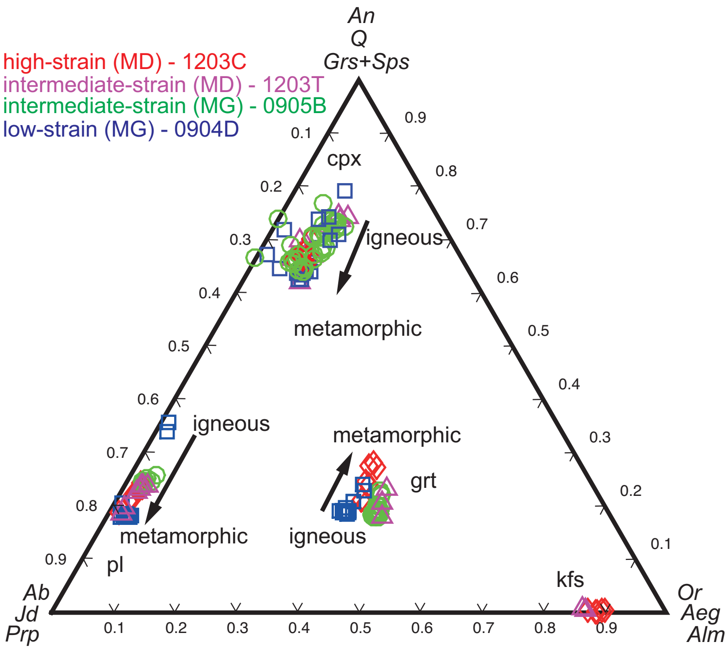

Chapman et al. Figure 9

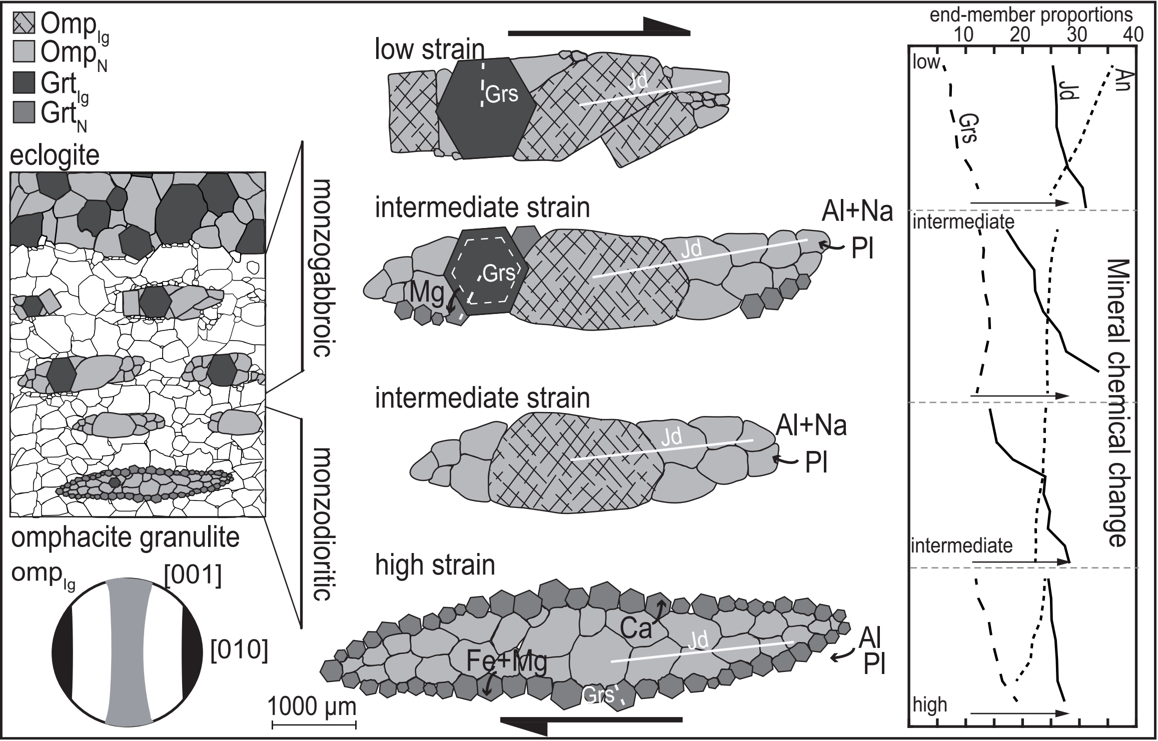

Chapman et al. Figure 10

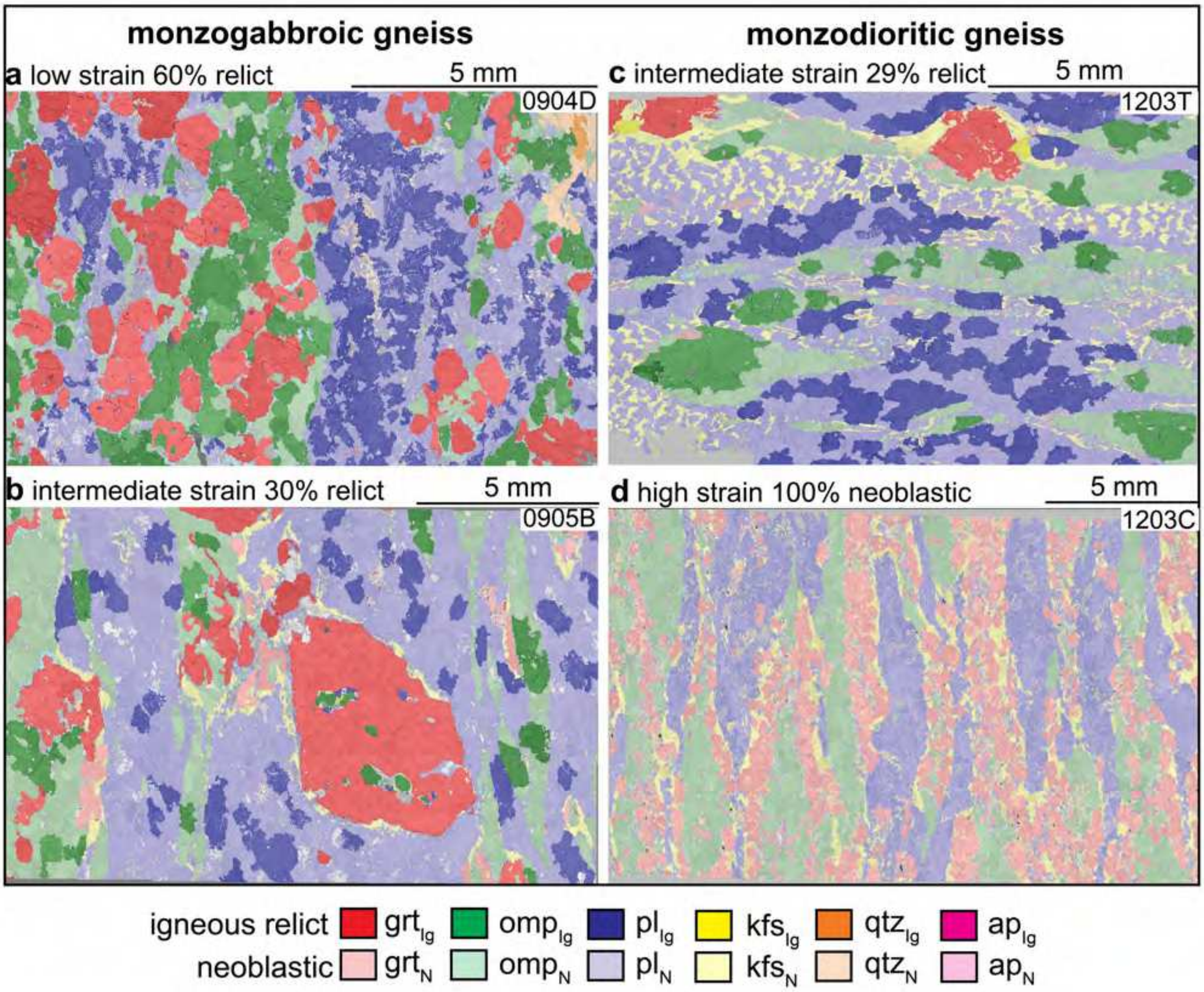

Chapman et al. Figure 11